On the role of surface deformation in the oxidation of NiCr alloys at 340–600 °C

Thomas Gheno, Clara Desgranges, Laure Martinelli

On the role of surface deformation in the oxidation of NiCr alloys at 340–600 °C

Thomas Gheno[a,b*], Clara Desgranges[a,c] and Laure Martinelli[a]

[a] *DEN-SCCME, CEA, Université Paris-Saclay, 91191 Gif-sur-Yvette, France*

[b] *DMAS, ONERA, Université Paris-Saclay, 92322 Châtillon, France*

[c] *Safran Tech, rue des jeunes bois, Châteaufort, 78772 Magny-les-Hameaux, France*

This is the accepted version of an article published in Corrosion Science, available at:
https://doi.org/10.1016/j.corsci.2020.108805

Abstract The effect of surface deformation on selective oxidation is studied on a Ni–30Cr alloy prepared by grinding (SiC paper) vs. polishing (diamond suspensions), and oxidized in air at 340–600 °C. Imaging and subsurface composition profiling by transmission electron microscopy are combined to investigate the relationships between microstructure, diffusion and oxidation. The depth of deformed material is found to be critical to selective oxidation. Atypical Cr depletion profiles reflect an abrupt change in diffusion properties between the severely deformed subsurface and the bulk. The relative contributions of grain boundary, dislocation and bulk diffusion to the Cr flux are examined based on short-circuit diffusion theory.

Keywords Ni-based alloys; cold work; selective oxidation; diffusion; dislocations; grain boundaries

1 Introduction

Heat-resisting austenitic steels and a number of Ni alloys rely on Cr-rich oxide scales for protection against various forms of high-temperature corrosion. Component surfaces are typically cold-worked during manufacturing, by a variety of techniques such as grinding, shot-peening or grit-blasting; this has been observed (and used) to improve their corrosion resistance. Surface cold working proceeds from a local form of severe plastic deformation. It produces a layer of nanocrystalline (also referred to as ultrafine-grained or UFG) material, with high dislocation densities [1–3]. Upon subsequent heating, the stored energy drives recovery and recrystallization, whereby dislocations rearrange to form subgrain and grain boundaries, and grain growth [4].

The general principle of the effect of cold work is that dislocations and grain boundaries in the deformed region act as fast diffusion paths, which increases the Cr flux to the surface and favors its selective oxidation. This effect is temperature-dependent. Three regimes are distinguished here: high (700–1000 °C), intermediate (400–700 °C) and low (250–400 °C) temperatures — this subdivision is arbitrary but would roughly cover cases ranging from mixed gas atmospheres in the chemical industry to steam and supercritical water or CO_2 in fossil power to pressurized water in nuclear power applications, respectively.

*Corresponding author. Email address: thomas.gheno at onera.fr

At high temperatures, cold work has generally been found to promote Cr_2O_3 formation [5–12] (although opposite results have also been reported [13]). This has been associated with accelerated Cr diffusion in the fine-grained zone resulting from recrystallization of the cold-worked material (in austenitic steels, deformation-induced martensite can also contribute). It has also been suggested that dislocations in the as-deformed microstructure play an important role in the early stages of oxidation at 900 °C, even as they are being annealed out [7]. This effect is necessarily short-lived, as recrystallization of austenitic alloys is rapid at these temperatures (in the order of minutes). In a study of NiCr oxidation in O_2 at 900–1100 °C, Giggins and Pettit [5] found that the oxidation behavior of grit-blasted specimens was the same whether or not they were annealed to induce recrystallization prior to oxidation. The role of cold work may then be viewed as akin to that of grain refinement — which is also known to promote Cr_2O_3 formation at high temperature [14–17].

At intermediate temperatures, recrystallization is slower (minutes to months), and the as-deformed microstructure has a longer lasting influence on the oxidation process. Depending on the conditions of interest, both the dislocations in the as-deformed state and the recrystallization-induced grain boundaries have been suggested to contribute to accelerated Cr diffusion [7,18–20]. Another significant aspect is that Cr-containing alloys tend to be more prone to internal and intergranular oxidation at these temperatures. Reducing the grain size may then have adverse consequences, as grain boundaries are fast diffusion paths for O as well as for Cr. In these conditions, grain refinement and cold work have generally been found to be beneficial to higher Cr grades, and to have either little effect or some detrimental effect on lower Cr grades [18,21–23].

At low temperatures, reports on the effect of cold work have shown significant variance even for similar conditions. While beneficial effects have been reported [24–28], a number of studies have found that cold-worked surfaces produced scales with lower Cr concentrations or higher growth rates than scales grown on their electropolished counterpart (see for instance [3,29,30] and refs. therein). In Refs. [31,32], oxide intrusions were observed below the surface scale of cold-worked steels, which the authors attributed to accelerated O diffusion along dislocations in the deformed microstructure. The role of grain boundaries is composition-dependent, as noted above for intermediate temperatures. In Ref. [33] for instance, grain boundaries were found to favor external Cr_2O_3 formation in alloy 690, and to promote intergranular oxidation in alloy 600. At low temperatures, recovery and recrystallization are so slow that the as-deformed microstructure may subsist for years. It is therefore expected to have a predominant role in selective oxidation. The specifics of this role are, however, not well documented.

The variability of the experimental observations regarding the role of cold work, especially at low and intermediate temperatures, points to a need for detailed investigations of cold-worked microstructures, and of the role of these microstructures on diffusion in the subsurface zone and consequently on selective oxidation. The present paper examines these questions based on the study of a model Ni–30Cr alloy, polished or ground, and oxidized in air at 340–600 °C. The particularity of the paper is the use of subsurface composition profiles measured by transmission electron microscopy (TEM) to study the relationships between microstructure, diffusion and oxidation.

2 Materials and methods

2.1 Materials

The experiments were run using a Ni–30Cr (wt. %) ingot, received in as-cast condition from Ugine-Savoie Imphy (supplier analysis: 30.4 wt. % Cr, main impurities (ppmw): 20 C, 2500 Fe, 200 Mn, 100 N, 9 S, 1000 Si). Plates cut from the ingot were subjected to cold-rolling and annealing to induce recrystallization and produce equiaxed microstructures. Two procedures, yielding finer and coarser grains, were used:

- rolling with 90 % reduction ($\varepsilon = 2.3$) followed by 20 h annealing at 725 °C, which produced 6 ± 3 µm grains (referred to as annealed, fine-grained);
- rolling with 56 % reduction ($\varepsilon = 0.8$) followed by 18 h annealing at 1075 °C, which produced 67 ± 39 µm grains (referred to as annealed, coarse-grained).

The grain sizes were measured by the intercept method from optical micrographs of cross-sections etched with a 1 HNO_3 – 1 HCl – 1 H_2O solution.

To produce oxidation specimens, the plates were first cold-rolled, then cut into 10 x 15 mm coupons, and suspension holes drilled. The coupons were then vacuum heat treated as indicated above. This procedure minimized cold-work due to machining. A series of coupons were also used in the as-rolled condition. These presented heavily deformed, elongated grains.

2.2 Surface preparation

Two surface preparation procedures were used, yielding heavier or lighter surface deformation. The specimens were either:

- ground with P500 grade SiC paper for 20 s (referred to as ground);
- or ground with P500, P1200 and P2000 SiC paper for 30 s each, and then polished with 9 µm, 3 µm and 1 µm diamond suspensions for 2, 4 and 6 min, respectively (referred to as polished).

The preparation was done using automatic polishing machines so as to ensure that the experimental conditions (load and duration) were kept constant. Specifically, the 20 s P500 SiC grinding step was done with an Abramin machine (Struers), applying a 120 N force to 3 specimens at a time (0.27 MPa), while the polishing steps were done with a Tegramin machine (Struers), applying a 20 N force on each specimen individually (0.13 MPa). For the polished specimens, the grinding steps were done manually.

Some of the specimens were analyzed by laser interferometry (Bruker Contour GT-K) at successive steps of the surface preparation process in order to monitor the evolution of the surface roughness. Values of the arithmetic mean roughness *Ra* were about 100–200 nm for the ground surfaces and 1–5 nm for the polished surfaces.

2.3 Oxidation experiments

The oxidation experiments were conducted in a tube furnace, with flowing dry (synthetic) air, at temperatures in the range 340–600 °C, for various durations (Table 1).

Table 1: Duration of the oxidation tests (in h).

Microstructure	Annealed, fine-grained		Annealed, coarse-grained		As-rolled
T (°C)\Surface	Ground	Polished	Ground	Polished	Polished
340	575	575			575
400	20 and 48	20 and 48	20	20	48
500	2	2	2	2	2
550			789	789	
600	1	1	1	1	

The durations were initially chosen so as to have comparable extents of oxidation at different temperatures, with little or no recrystallization. A longer run was added at 550 °C so as to study the alloy subsurface after significant recrystallization.

The furnace was calibrated with a type K thermocouple. The gas flow rate was 30 ml/min (0.6 mm/s at 500 °C). To start the experiments, the furnace was first stabilized at the desired temperature. The specimens were suspended to a quartz holder using quartz hooks, and placed into a cold zone of the furnace tube. The tube was flushed with dry air for 2 h. The sample holder was then pushed into the hot zone using a rod passing through a polymer end-cap. This allowed rapid heating of the specimens. At the end of the experiment, the sample holder was pulled back to the cold zone. Heating and cooling rates were not specifically measured for these experiments, but based on previous measurements in a similar configuration, they are estimated to be about 3 K/s on average.

Oxide thickness and composition were analyzed by glow discharge optical emission spectroscopy (GDOES) on all oxidized specimens, while in-depth analysis by TEM was conducted on selected specimens, due to practical constraints.

2.4 GDOES analysis

Composition-depth profiles were measured in the oxidized specimens by GDOES using a GD-Profiler 2 from Horiba Jobin-Yvon. The profiles were recorded by sputtering from the specimen surface through the oxide scale, into the substrate. The signal was collected from a 4 mm diameter area. The sputtering rate was found to vary significantly depending on the grain orientation. This was a problem in the metal, even for the fine-grained specimens, as the variable sputtering rate generated important roughness at the bottom of the sputtering crater, and resulted in poor depth resolution ($>$ 100 nm). As a consequence, GDOES could not be used to study Cr depletion in the metal, and was only used to measure the composition and thickness of the oxide layers. The oxide thickness was subject to important local variations, as shown subsequently in TEM observations. The GDOES values represent an average over a large sampling area (4 mm diameter). The associated uncertainty depends on the thickness variations more than on the technique itself, and could not be quantified. These results should thus be considered approximate.

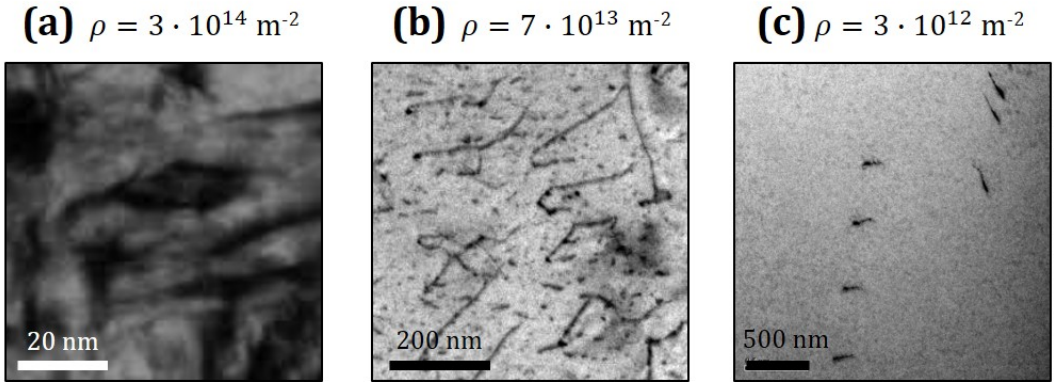

Figure 1: Examples of TEM images used for dislocation density measurements. (a) High dislocation density; (b) intermediate dislocation density; (c) low dislocation density.

2.5 TEM analysis

As-prepared polished and ground specimens, as well as selected oxidized specimens, were analyzed by TEM. Electron-transparent foils were prepared by focused ion beam milling with a FEI Strata Dual Beam 400, and TEM analysis was conducted on a FEI Tecnai Osiris equipped with ChemiSTEM EDS detector and ASTAR precession diffraction system from Nanomegas. The TEM specimen preparation and analysis were carried out by SERMA Technologies in Grenoble, France.

In order to study the relationships between microstructure and oxidation, bright field and dark field images, as well as EDS analyses and precession diffraction, were combined. Composition profiles were measured by EDS with a step size of 0.5 to 5 nm. Dislocation densities (ρ) were measured from images obtained in weak beam mode: their length was measured in an image processing software, and for each image the cumulated length was divided by the corresponding volume (average foil thicknesses were determined by SEM at the end of the milling process). In the dislocation density profiles presented in the paper, each point corresponds to one image. Two main difficulties were encountered: in strongly deformed zones ($\rho > 10^{14}$ m^{-2}), dislocations were numerous and difficult to distinguish, and had to be observed with high magnification (see Fig. 1a), which reduced the volume sampled in one image. In zones with small dislocation densities ($\rho < 10^{13}$ m^{-2}), lower magnification images were used, but the number of dislocations sampled in one image was also limited (Fig. 1c). For these reasons, the ρ values given in the paper should be considered approximate.

3 Experimental results

3.1 Initial surface microstructures

Polished specimen

Polishing the annealed alloy produced surfaces with very little deformation, as shown in Fig. 2a. However, close examination shows a row of elongated grains about 100 nm wide and 30 nm deep directly below the surface (Fig. 2b and c). Dark field imaging

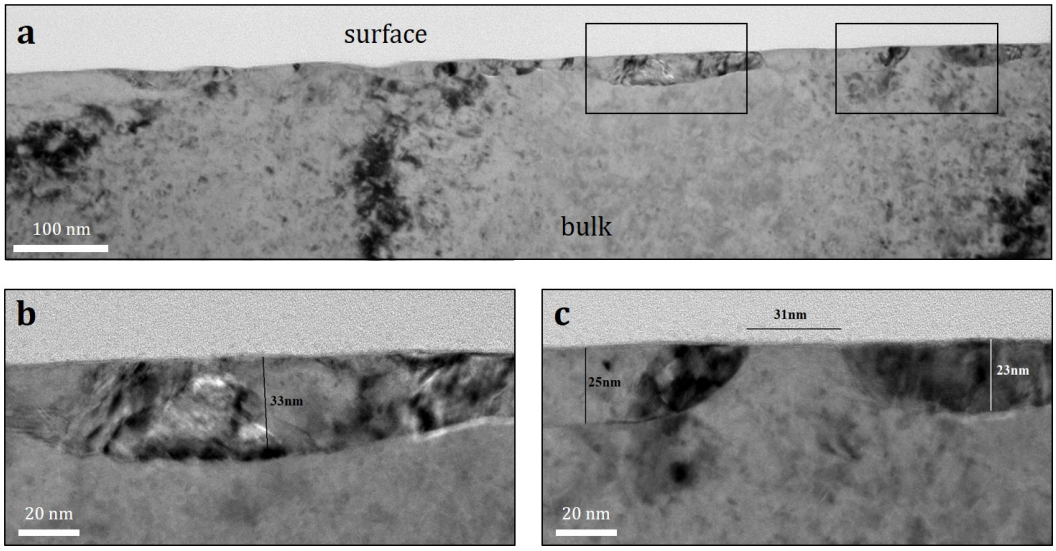

Figure 2: Bright field TEM images of the near-surface microstructure of Ni–30Cr (annealed, fine-grained) after 1 µm polishing. (a) Overview; (b) and (c) zoomed view of boxed areas in (a) showing the surface deformed layer.

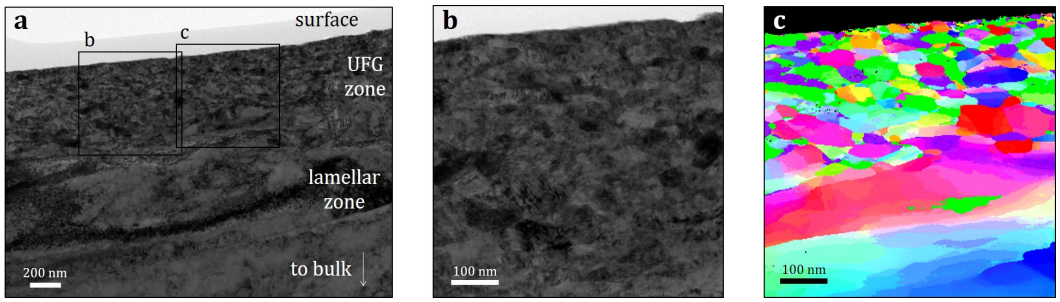

Figure 3: TEM observation of the near-surface microstructure of Ni–30Cr (annealed, coarse-grained) after P500 SiC grinding. UFG: ultrafine-grained. (a) Bright field overview; (b) bright field image of UFG zone; (c) orientation map in UFG zone obtained by PED.

with varying tilt angles (not shown here) indicated that these were indeed grains with crystallographic orientations distinct from that of the underlying alloy.

The dislocation density was found to be much larger in these surface grains than in the bulk (on average 4×10^{14} m^{-2} vs. 2×10^{12} m^{-2} in the bulk). In summary, mechanical polishing with 1 µm particles produced a shallow but distinctive cold-worked region at the specimen surfaces.

Ground specimen

Grinding produced more extensive deformation, as shown in Fig. 3. A zone about 300 nm deep made of 10–30 nm grains is found immediately below the surface (referred to as ultrafine-grained, or UFG zone). Further down, the microstructure is lamellar, with larger and elongated grains, over a depth of about 0.5–1 µm. Deeper still, the grain morphology is visibly less affected by the grinding treatment.

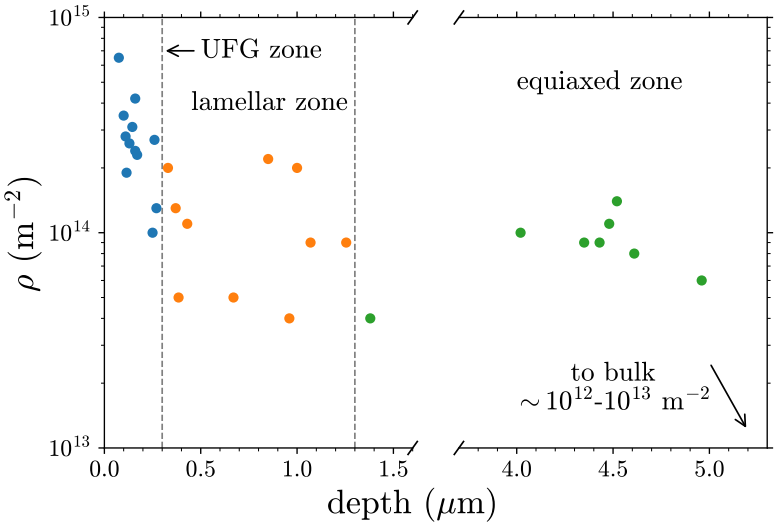

Figure 4: Dislocation density-depth profile measured in annealed (coarse-grained), ground Ni–30Cr specimen.

The ground surface was analyzed by precession electron diffraction (PED, Fig. 3c), which confirmed that the UFG zone was indeed made of distinct grains formed by nanocrystallization during the grinding treatment. Dislocation densities measured at varying depths are presented in Fig. 4. Values obtained in the UFG zone are high (10^{14}–10^{15} m^{-2}), similar to those measured at the surface of the polished specimen. Deeper in the specimen, ρ values remain large: about 10^{14} m^{-2} in the lamellar and equiaxed zones, which is 50 times higher than in the bulk of the polished specimen (2×10^{12} m^{-2}) — grinding affected the alloy microstructure over a depth larger than that of the TEM foil (5 µm).

3.2 Oxidation results

General oxidation behavior

Depth profiling by GDOES was used to measure the approximate composition and thickness of the oxide scales formed in the oxidation experiments. The specimens formed two-layer scales, with Cr-rich oxide at the alloy-scale interface and Ni-rich oxide at the scale-gas interface. At a given temperature, the microstructure and surface preparation did not significantly influence the total scale thickness, but did have an effect on the relative thicknesses. On the ground specimens, the Ni oxide was 1–2 nm thick, which made up less than 10 % of the total thickness: the scale was essentially Cr oxide. On the polished specimens, however, the proportion of Ni oxide was between 1/4 and 1/2 of the total. These trends are illustrated in Fig. 5, which shows the thicknesses obtained for a series of fine-grained and as-rolled specimens after oxidation at 340, 400 and 500 °C.

The oxide scale and underlying metal were studied by TEM on three specimens: one oxidized 48 h at 400 °C, which showed little recrystallization, and two oxidized 789 h at 550 °C, which were subject to significant recrystallization. This is presented in the next Sections.

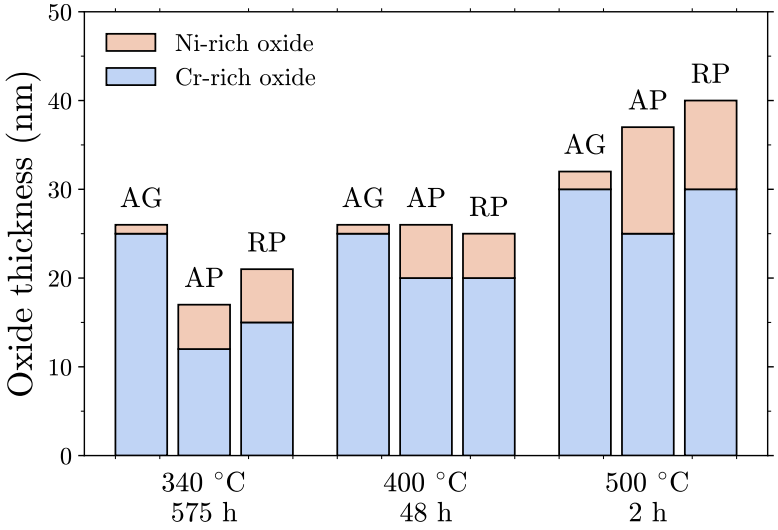

Figure 5: Oxide layer thicknesses estimated from GDOES composition profiles after oxidation of Ni–30Cr in dry air in the indicated conditions. AG: annealed (fine-grained), ground; AP: annealed (fine-grained), polished; RP: as-rolled, polished. Each bar represents one specimen. Note that the values reflect signal collected over a large analysis area (4 mm diameter); as shown subsequently, the oxide layers had uneven thicknesses.

Polished specimen oxidized at 550 °C

Oxidation of the polished alloy at 550 °C produced two-layer scales (Fig. 6). No internal oxidation was observed. Analysis by EDS indicated that the oxides in the outer and inner layer had the composition of NiO and Cr_2O_3, respectively. Both layers were found to have highly variable thicknesses, with values ranging from 10 to 300 nm. The inner layer had a variable morphology, from thin and dense to thick and highly porous, as shown in Fig. 6a and b. Some of the pores in the Cr_2O_3 layer contained Ni-rich oxide. This is illustrated in the EDS maps of Fig. 6c, where Ni-rich oxide particles are seen on the walls of the pores.

Figure 7 shows a bright field image and associated phase map obtained by PED, which confirmed the crystallographic nature of the oxide phases. Both NiO and $NiCr_2O_4$ spinel are identified around pores in the Cr_2O_3 layer. Examination of the PED results confirmed the high variability of the oxide grain size, from less than 10 nm to 200 nm.

Composition profiles were recorded by EDS across and below the oxide scale in 6 different zones of the specimen. All profiles showed Cr depletion in the metal, with a shape typical of selective oxidation, as shown in Fig. 8.

The dislocation density measured immediately underneath the scale was similar to that in the bulk of the specimen, about 4×10^{12} m^{-2} on average, which is similar to the value measured in the bulk before oxidation.

Ground specimen oxidized at 550 °C

Oxidation of the ground alloy at 550 °C produced a single oxide layer, shown by EDS to be Cr_2O_3. The scale thickness was found to vary between 100 and 300 nm (except

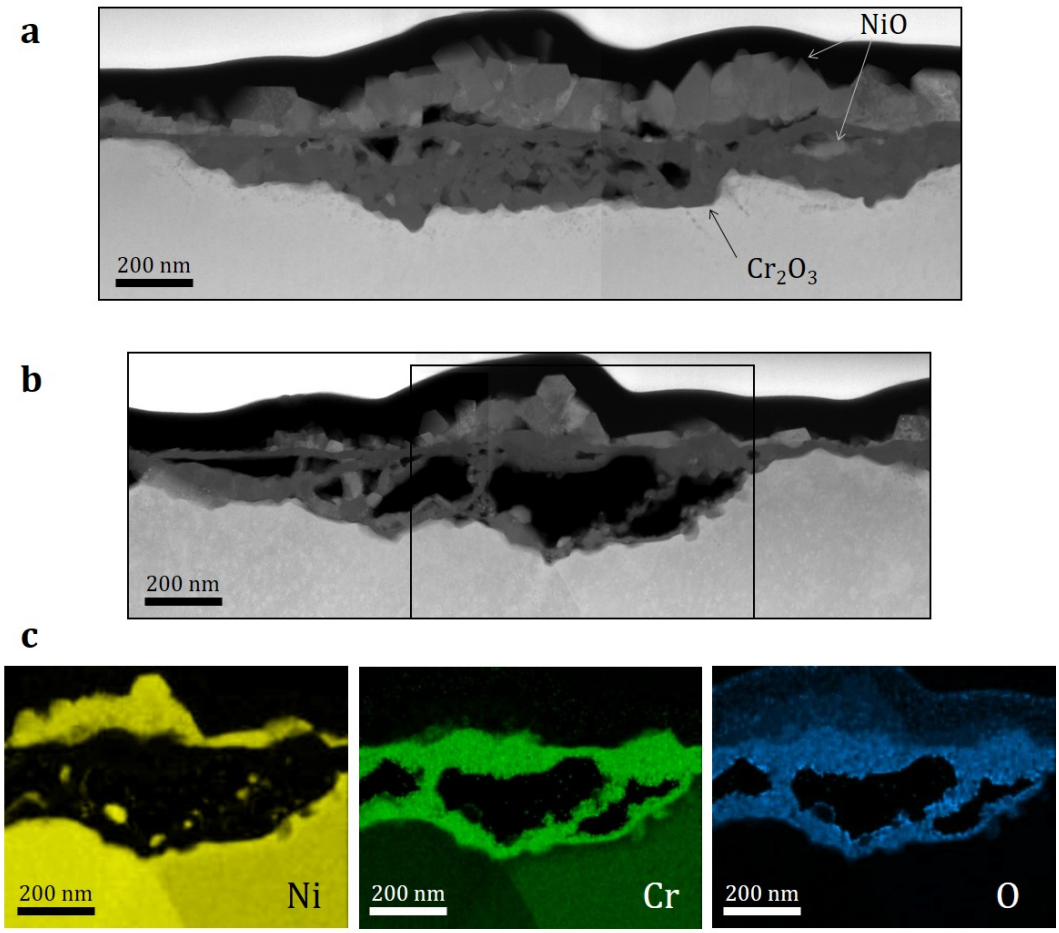

Figure 6: Annealed (coarse-grained), polished Ni–30Cr coupon after 789 h at 550 °C in dry air. (a, b) Dark field STEM images, showing varying extents of porosity in the inner layer; (c) EDS maps from the boxed area in (b).

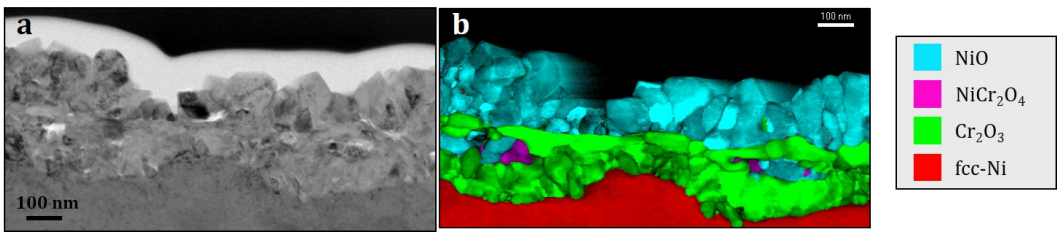

Figure 7: Annealed (coarse-grained), polished Ni–30Cr after 789 h at 550 °C in dry air. (a) Bright field TEM image; (b) composite phase and index map of (a) obtained by PED.

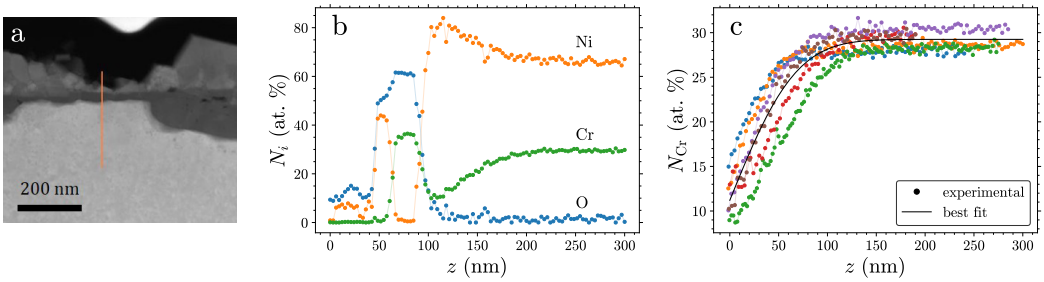

Figure 8: (a) Dark field STEM image of annealed (coarse-grained), polished Ni–30Cr after 789 h at 550 °C in dry air; (b) concentration profiles measured by EDS along line in (a); (c) Cr concentration profiles measured along line in (a) and in 5 other locations of the same specimen, with fitted profile superimposed (see Section 4.1).

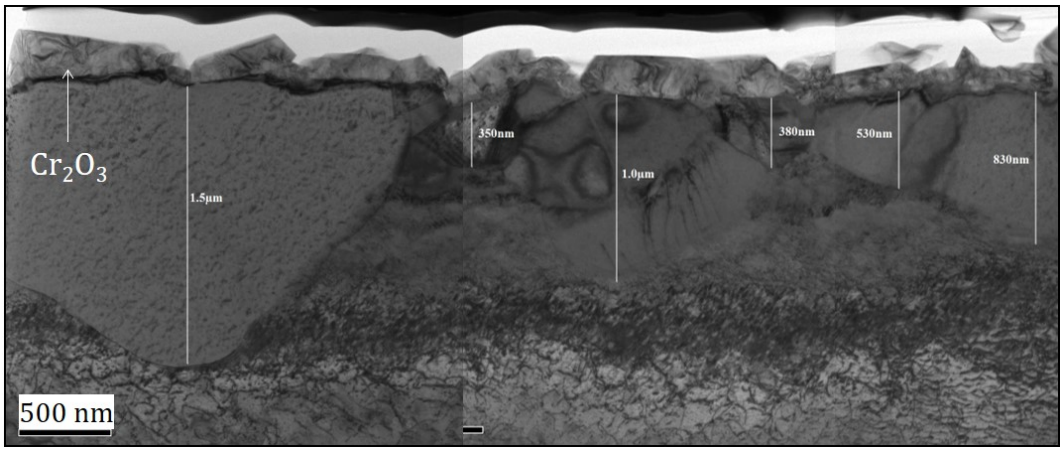

Figure 9: Bright field TEM image of annealed (coarse-grained), ground Ni–30Cr after 789 h at 550 °C in dry air, showing recrystallized zone below Cr_2O_3 scale.

for a few larger oxide grains). The oxidation heat-treatment caused recrystallization in the grinding-induced deformed zone, as shown in Fig. 9. The new grains are between 300 nm and 1.5 µm large and have a relatively low dislocation density (similar to the annealed material). Remarkably, the dislocation densities measured immediately below the annealed zone are still quite high, and values typical of the annealed material are only recovered at depths over 15 µm, as shown in Fig. 10.

Composition profiles were measured by EDS across and below the oxide scale in 4 different zones of the specimen. All profiles showed Cr depletion in the metal, albeit with an unusual shape: the Cr concentration is constant, at 22–26 at. %, over some depth, and then steeply returns to the bulk value. The Cr-depleted plateau was found to coincide with the recrystallized zone, as illustrated in Fig. 11.

Polished specimen oxidized at 400 °C

Oxidation of the polished alloy at 400 °C produced two-layer scales, as shown in Fig. 12. Analysis by EDS indicated that the oxides had the composition of NiO and Cr_2O_3. The Cr_2O_3 layer had a relatively constant thickness of about 10 nm, while the NiO layer thickness was highly variable, from 3–4 nm in general to 50

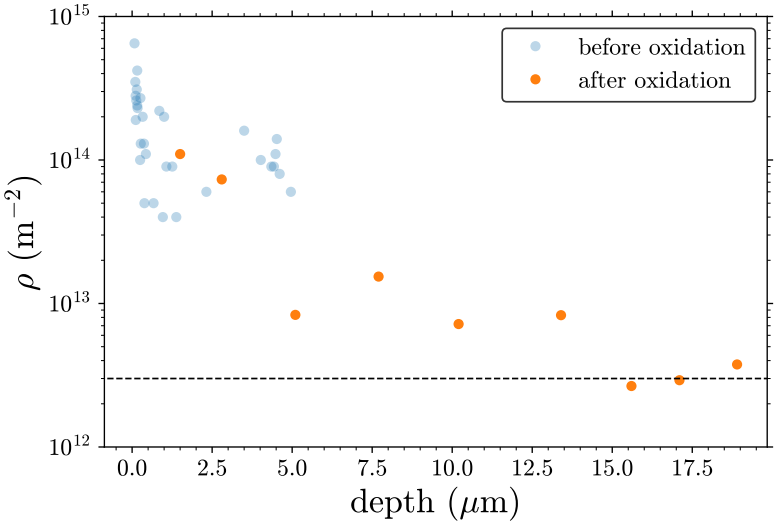

Figure 10: Dislocation density-depth profile measured in annealed (coarse-grained), ground Ni–30Cr specimen after 789 h at 550 °C in dry air. The value representative of annealed material is indicated by the dashed line. The values measured before oxidation (Fig. 4) are included for comparison.

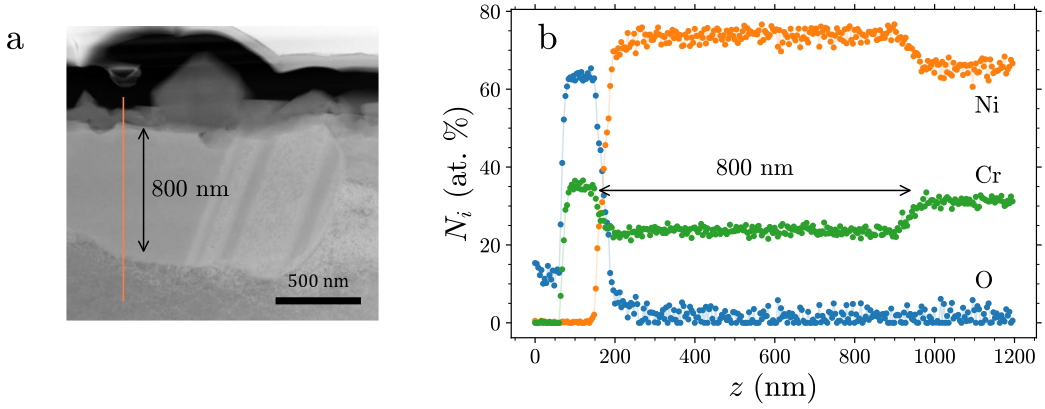

Figure 11: (a) Dark field STEM image of annealed (coarse-grained), ground Ni–30Cr after 789 h at 550 °C in dry air; (b) concentration profiles measured by EDS along line in (a).

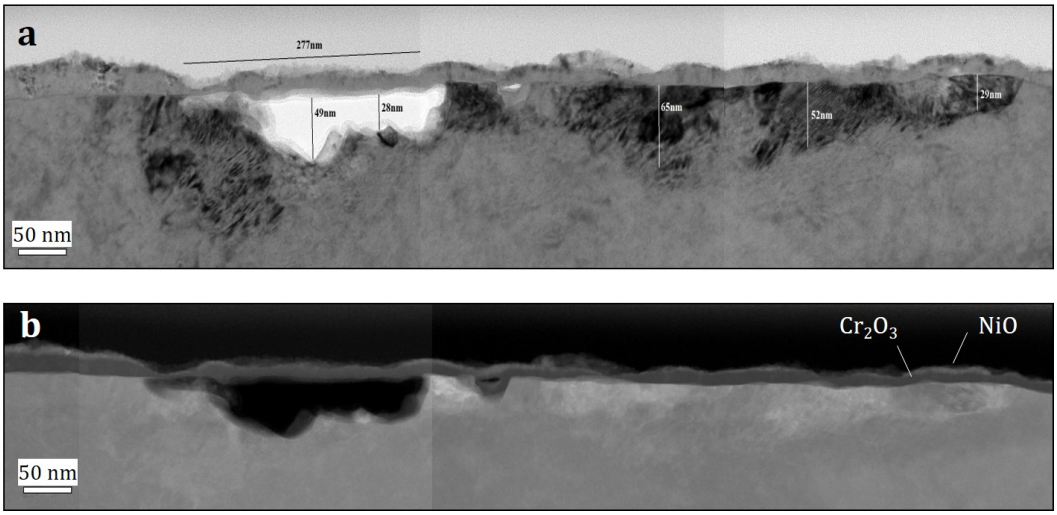

Figure 12: Observation of annealed (fine-grained), polished Ni–30Cr after 48 h at 400 °C in dry air. (a) bright field TEM image showing large cavity and partially recrystallized substrate below the oxide scale; (b) dark field STEM image of the same area, showing Cr_2O_3 and NiO layers.

nm locally. Contrary to what was observed after oxidation at 550 °C, the Cr_2O_3 layer appeared to be dense. However, pores about 50 nm deep and 200 nm long (see Fig. 12) were found all along the metal/oxide interface, with an average inter-pore spacing of 1.5 µm. The pores were either empty or partially filled with oxide. Some oxide regions were observed below the Cr_2O_3 layer with shapes and dimensions similar to those of the pores, suggesting that some pores had been fully filled with oxide. Fig. 13 shows EDS maps recorded in a zone with a partially filled pore. The material inside the pore is seen to be mostly Ni oxide, with some Cr oxide at the alloy surface.

The Cr signal below the oxide scale in the EDS map of Fig. 13 shows variations along the interface. Chromium depletion was further investigated using composition profiles — three examples are shown in Fig. 14. Out of 12 recorded profiles, 8 showed no or very little Cr depletion (as in Fig. 14d), while 4 had a tub-shape similar to that observed in the 550 °C ground specimens, with a more or less flat zone of heavy Cr depletion (as in Fig. 14b and c). In these profiles, the size of the Cr-depleted zone was about 30 nm, similar to the depth of the deformed grains. However, some of the tub-shaped profiles were recorded in zones with no visible deformation.

The ultrafine, highly deformed grains created by polishing were mostly still visible after oxidation, although part of the subsurface appeared to be deformation-free, suggesting that some had recrystallized and merged with the underlying substrate grains (compare Figs. 12a and 14a with Fig. 2). In the remaining deformed grains, however, the dislocation density was about 3×10^{14} m^{-2} on average, close to the values measured before oxidation (see summary in Table 2).

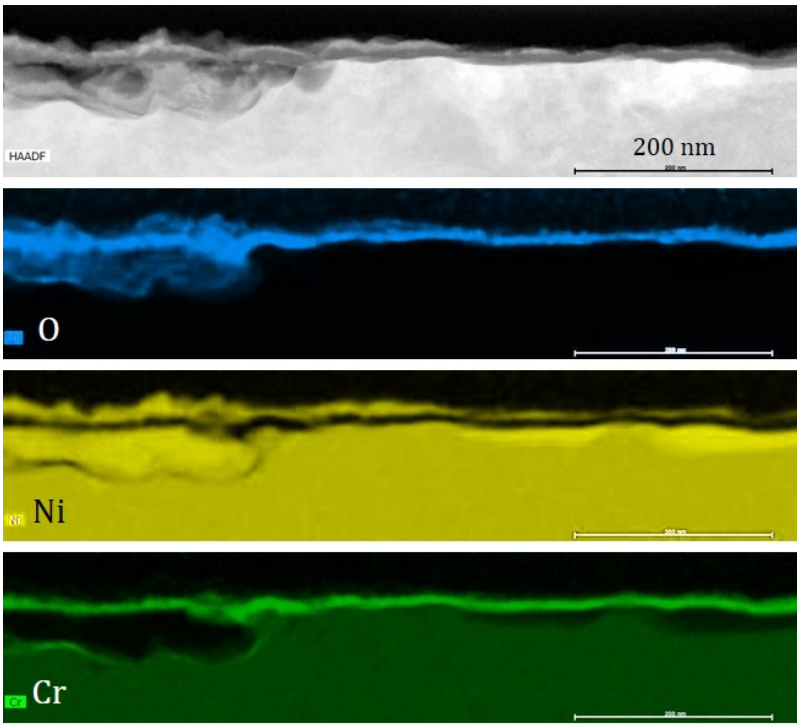

Figure 13: HAADF STEM image and corresponding EDS maps (O, Ni and Cr) of annealed (fine-grained), polished Ni–30Cr after 48 h at 400 °C in dry air.

Table 2: Average dislocation densities (ρ, m^{-2}) measured in the cold-worked and bulk regions of Ni–30Cr specimens.

	Annealed, polished		Annealed, ground	
	UFG zone (< 30 nm)	bulk	UFG zone (< 300 nm)	bulk
As-prepared	4×10^{14}	2×10^{12}	3×10^{14}	n/a[a]
Oxidized				
48 h at 400 °C	3×10^{14}	3×10^{12}		
789 h at 550 °C	n/a[b]	4×10^{12}	n/a[c]	3×10^{12}

[a]Bulk zone not present in TEM foil
[b]UFG zone consumed by oxidation
[c]Too small to be measured

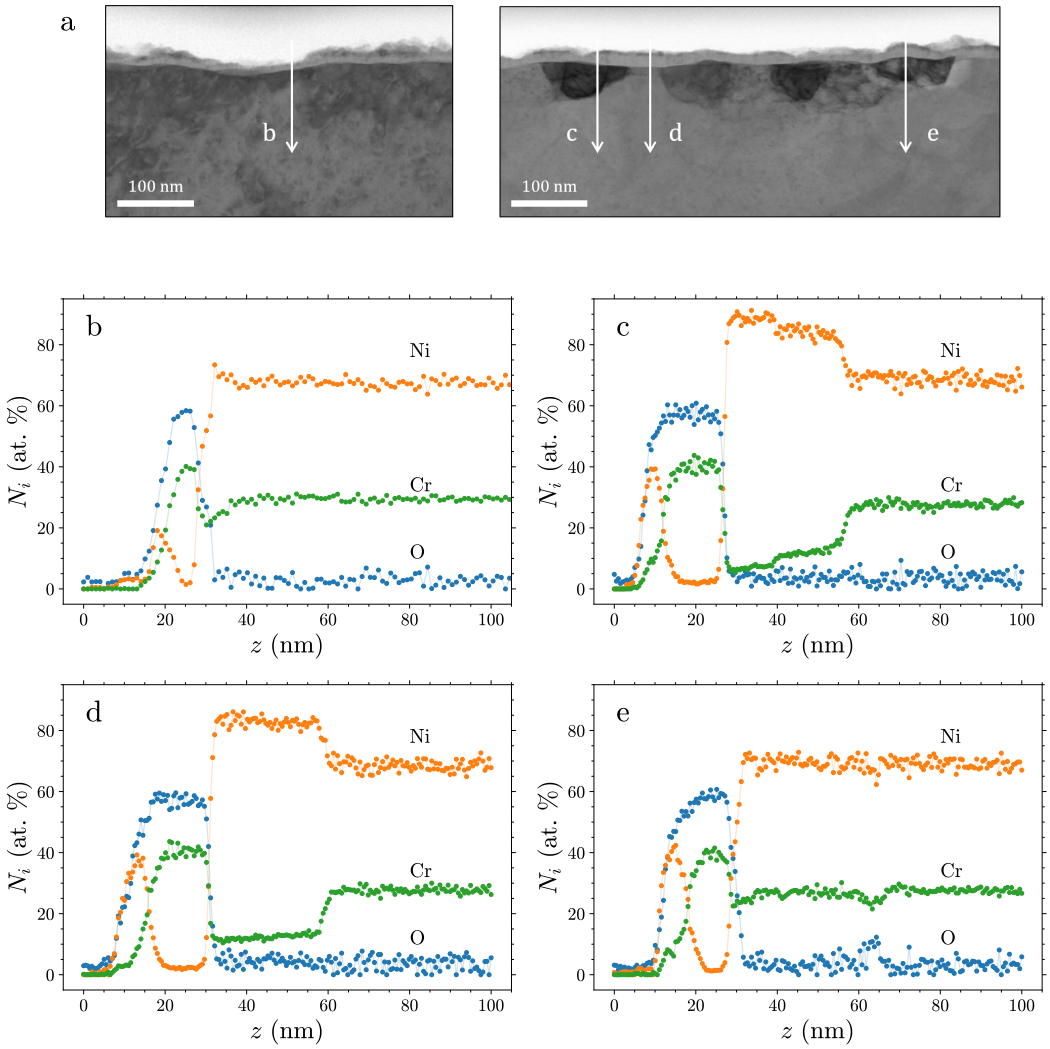

Figure 14: Analysis of Cr depletion in annealed (fine-grained), polished Ni–30Cr after 48 h at 400 °C in dry air. (a) Bright field STEM images; (b), (c), (d) and (e) concentration profiles measured by EDS along the arrows in (a).

4 Discussion

The microstructures produced by either polishing or grinding contain a UFG zone with ∼ 20 nm grains and large dislocation densities (Table 2). The formation of the UFG zone results from surface nanocrystallization during the surface preparation; it can be seen as a type of dynamic recrystallization. As the process continuously generates new dislocations, the dislocation density remains large in the new grains.

Polishing and grinding produced UFG zones with similar grain sizes and dislocation densities (compare Figs. 2 and 3, see Table 2). The UFG zone extends much deeper in the ground specimens, however. This provides a much larger volume of high-diffusivity material. In addition, ground surfaces are rougher than polished surfaces, which may also affect selective oxidation, in particular in its early stages. The beneficial consequence of grinding is evident in the 550 °C experiment: the ground

specimen formed a Cr_2O_3 scale (Fig. 11), while the polished specimen formed a two-layer NiO / Cr_2O_3 scale (Figs. 6 and 7). A detailed analysis of the ground specimen oxidized at 400 °C is not available, but the GDOES results indicate that grinding also led to a slight reduction of NiO thickness at this temperature, compared to polishing (Fig. 5). Nevertheless, upon oxidation of the polished specimen at 400 °C, diffusion was accelerated in the shallow UFG zone (at least locally, see Fig. 14) and the scale was predominantly Cr_2O_3 (Figs. 12–14). Although we do not know how a deformation-free surface would have oxidized, accelerated Cr diffusion in the shallow UFG zone presumably helped produce a quasi-exclusive Cr_2O_3 scale in the polished specimen at 400 °C.

The following Sections examine the role of the deformation-induced microstructure in diffusion and selective oxidation, based on the measured composition profiles and on the classical theory of grain boundary and dislocation diffusion, starting with the 550 °C specimens. The discussion then addresses some peculiar aspects of the oxidation mechanism.

4.1 Microstructure and shape of the Cr depletion profiles at 550°C

In his analysis of selective oxidation, Wagner showed that selective oxidation, i.e., the formation of an external oxide scale of the less noble element with no oxidation of the base metal, is achieved when the outward flux of the less noble element (i) overcomes the inward O flux, thereby avoiding internal oxidation [34], and (ii) matches the flux required for scale growth, thereby avoiding the oxide reduction by the base metal [35]. As shown in the Appendix, if only bulk diffusion is considered, a Ni–30Cr alloy is far from meeting either of these two criteria at the temperatures of interest (300–600 °C), and is thus expected to undergo non-selective oxidation.

The polished 550 °C specimen provides an illustration of this, as it formed significant amounts of NiO alongside Cr_2O_3. The role of the microstructure in the failure to avoid NiO is reflected in the Cr depletion profiles measured underneath the 2-layer scale. Assuming that (i) the specimen is semi-infinite, (ii) the alloy composition at the metal/oxide interface remains constant throughout the oxidation, (iii) the diffusion coefficient of Cr and the molar volume of the metal are composition-invariant, and (iv) neglecting the recession of the metal, the solution of the diffusion equation in a single-phase medium is written [36]:

$$\frac{N(x,t) - N_b}{N_i - N_b} = \mathrm{erf}\left(\frac{x}{2\sqrt{\widetilde{D}t}}\right) \tag{1}$$

where N is the Cr atom fraction, i and b denote the interfacial and bulk values, respectively, x is the distance into the alloy from its original surface, t is the time and $\widetilde{D}$ is the interdiffusion coefficient. Equation (1) was fitted to the experimental profiles in Fig. 8c by adjusting $\widetilde{D}$ and N_i, with a least-squares method. (Note that this use of Eq. (1) is by no means predictive: N_i depends on the NiO and Cr_2O_3 thicknesses, which are not predicted here. The Eq. is only used to estimate the rate of Cr diffusion in the alloy.) This yielded an average $\widetilde{D} = (5.0 \pm 2.9) \times 10^{-18}$ cm^2/s ($\pm$ one standard deviation on 6 profiles). This value is close to the expected $\widetilde{D}$ in γ-NiCr solid solutions at 550 °C, about 4×10^{-18} cm^2/s in the range 10–30 at. % Cr, calculated using Thermo-Calc [37] and the TCNI8 and MOBNI5 databases.

Table 3: Summary of defect diffusion regimes [39,40]. D_v: volume diffusion coefficient; λ_i: average spacing for defect i ($i = gb$ for grain boundaries or d for dislocations): $\lambda_{gb} = g$ (grain size) and $\lambda_d = 1/\sqrt{\rho}$, with ρ the dislocation density; ε_i: defect size: $\varepsilon_{gb} = \delta$ (grain boundary width) and $\varepsilon_d = a$ (dislocation core radius) — both δ and a are assumed to be 0.5 nm, as customary in fcc metals [39,40].

Regime	Condition	Parameters	Physical description	Diffusion properties
A	$\sqrt{D_v t} > \lambda_i$	High temperature Long time	Atoms visit many grains and gb's/dislocations; quasi-uniform diffusion front, as in homogenous media.	Effective diffusion coefficient (weighed average of volume and gb/dislocation diffusion coefficients).
B	$\varepsilon_i \ll \sqrt{D_v t} \ll \lambda_i$	Intermediate temperature Intermediate time	Atoms diffuse along gb's/dislocations and into volume, but diffusion fringes due to neighboring defects do not overlap.	Non-uniform.
C	$\sqrt{D_v t} < \varepsilon_i$	Low temperature Short time	Bulk diffusion is insignificant; diffusion occurs along gb's/dislocations.	Gb/dislocation diffusion coefficient (weighed by cross-sectional area fraction).

The assumptions made in using Eq. (1) are not quite met in practice, but the conclusion is clear nonetheless: the profiles measured in the polished specimen reflect bulk diffusion. At 550 °C, the shallow UFG zone produced by polishing is quickly consumed by oxidation, bulk diffusion prevails and selective oxidation cannot be achieved.

On the contrary, Cr depletion in the ground 550 °C specimen does not conform to the typical error function shape, and it extends much deeper into the alloy — much deeper than bulk diffusion would allow. The fact that the Cr depletion plateau coincides with recrystallized grains further indicates that Cr diffusion was accelerated by defects in the cold-worked zone. Questions of interest, then, concern the nature of the predominant defect (dislocations vs. grain boundaries) and the type of contribution these defects have on diffusion (localized vs. uniform).

4.2 Contributions from grain boundaries and dislocations at 550 °C

These questions can be addressed on the basis of the kinetic regimes introduced by Harrison for dislocation pipe diffusion [38] and later extended to grain boundary diffusion [39,40]; these are summarized in Table 3. Subregimes have been devised for grain boundary diffusion in coarse and finer polycrystals [39–41], but the general principles remain unchanged. Two major approximations are made here: Cr segregation in grain boundaries and dislocations is neglected, and all diffusion coefficients are treated as composition-invariant.

Using tracer diffusion data for Cr in Ni-20Cr from Ref. [42], $\sqrt{D_v t}$ is calculated to be 20 nm after 789 h at 550 °C. In the UFG zone of the ground specimen, the grain size is initially 20 nm on average, and reaches about 1 µm after 789 h at 550 °C (Fig. 9). It follows that $\sqrt{D_v t} < \lambda_{gb}$ from the beginning to the end of the experiment (λ_{gb} denotes the average defect spacing, approximated by the grain size), and it is concluded that grain boundary diffusion exceeds the C regime at some point but

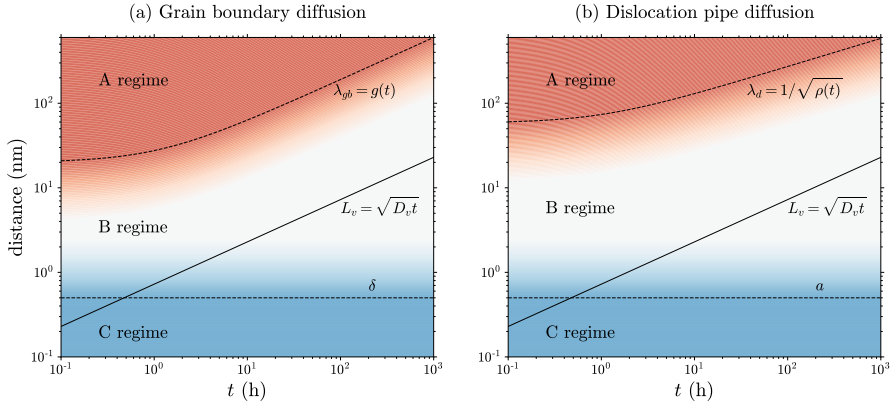

Figure 15: Comparison of the characteristic bulk diffusion distance with the defect size and the average defect spacing in the cases of (a) grain boundary diffusion and (b) dislocation pipe diffusion, at 550 °C. The A regime is not reached in either case within 1000 h. See text for details.

does not reach the A regime during the experiment, i.e., diffusion fringes from two neighboring grain boundaries do not overlap. If, for the sake of illustration, grain growth is modeled using parabolic kinetics: $g^2 - g_0^2 = k_g t$, and g_0 and k_g are adjusted to match the observed grain sizes in the UFG zone, the time evolution of the bulk diffusion distance and grain size can be compared; this is done in Fig. 15a.

The same approach is now applied to dislocation diffusion. The dislocation density (noted ρ) in the UFG zone of the ground specimen is initially about 3×10^{14} m^{-2}, which corresponds to $\lambda_d = 1/\sqrt{\rho} = 60$ nm. A ρ value could not be obtained after oxidation because the number of dislocations was too small in the surface grains, but using the bulk value of 3×10^{12} m^{-2} (Table 2), one obtains $\lambda_d = 600$ nm. It follows that $\sqrt{D_v t} < \lambda_d$, which indicates that dislocation diffusion operates in the B regime, i.e., dislocations act in an isolated manner. Again for the sake of illustration, recovery kinetics are described with a model of shape $\rho^{-3/2} \propto t$ [4], adjusted to match the ρ values measured at 550 °C; the time evolution of $\sqrt{D_v t}$ and λ_d are compared in Fig. 15b.

It is of interest to compare the contributions of grain boundaries and dislocations to the diffusion process. From the above estimations, it appears that in the UFG zone of the ground specimen, the average defect spacing for grain boundaries and dislocations are of similar magnitudes: $\lambda_{gb} \sim \lambda_d$, both in the as-deformed state and after 789 h at 550 °C. This is illustrated in Fig. 16a, which maps the λ_{gb}/λ_d ratio in the (g, ρ) space. The ratio is seen to tend toward values larger than 1 as recovery, recrystallization and grain growth proceed (i.e., diffusing atoms become more likely to encounter a dislocation than a grain boundary).

It is noted that although we consider time-dependent defect densities, this description remains static, in the sense that defect mobilities are not taken into account. The movement of dislocations and grain boundaries during recovery, recrystallization and grain growth may influence diffusion, both because it affects the rate at which diffusing atoms encounter defects, and via drag effects.

Furthermore, the λ_{gb}/λ_d ratio does not quite capture the relative contributions of the defects to diffusion, as it does not factor in the diffusivity associated with each

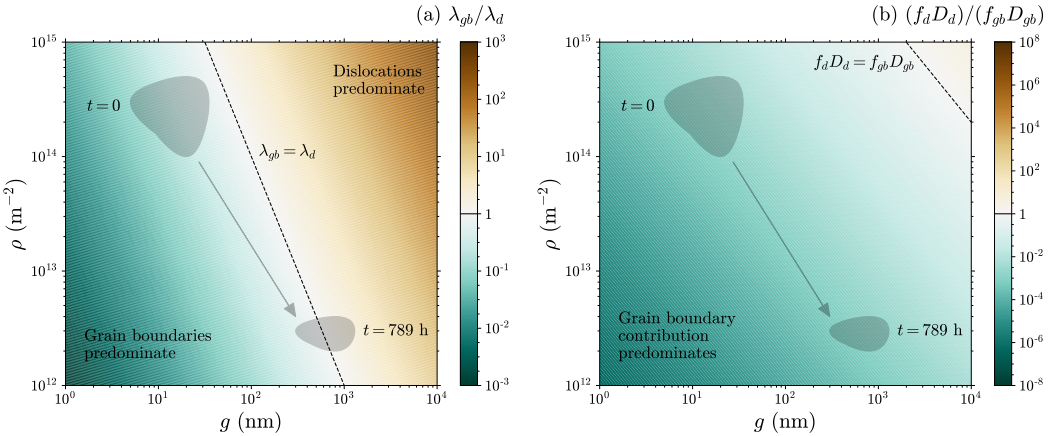

Figure 16: Maps of (a) λ_{gb}/λ_d and (b) $(f_dD_d)/(f_{gb}D_{gb})$ as a function of grain size and dislocation density, reflecting the relative contributions of grain boundaries and dislocations to defect density and defect diffusion, respectively. The diffusion data corresponds to $T = 550$ °C. The greyed areas correspond to grain sizes and dislocation densities measured in the UFG zone of the ground Ni–30Cr specimen, in the as-deformed state and after 789 h at 550 °C. See text for details.

type of defect. This can be estimated by considering the $(f_dD_d)/(f_{gb}D_{gb})$ ratio, where f_i is the cross-sectional surface area fraction (normal to the main diffusion direction) of defect i: $f_{gb} = \delta/g$ and $f_d = \pi a^2 \rho$, with δ the grain boundary width and a the dislocation core radius (different variants exist for f_{gb} depending on the grain morphology [39,40], but this level of detail is not useful here). Grain boundary diffusion data for Cr in various NiCr alloys reported in Ref. [43] are used to calculate $D_{gb} = 1.8 \times 10^{-11}$ cm^2/s at 550 °C and 25 at. % Cr (center of the composition range of interest, see Fig. 11b). Dislocation diffusion data for Cr in Ni are not available, to the best of our knowledge; instead, Ni dislocation self-diffusion data from the assessment in Ref. [44] are used, which yields $D_d = 5.6 \times 10^{-12}$ cm^2/s at 550 °C. These coefficients are used to calculate the $(f_dD_d)/(f_{gb}D_{gb})$ ratio, shown in Fig. 16b. The ratio is smaller than one in the conditions of interest, which indicates that grain boundary diffusion predominates.

It is also noted that the λ_{gb}/λ_d and $(f_dD_d)/(f_{gb}D_{gb})$ ratios represent relative contributions to defect density and defect diffusion; these become less relevant as time progresses, since bulk, rather than defect diffusion, will eventually predominate in the overall Cr flux. The amount of Cr that has diffused directly to the surface via the bulk exceeds the amount that has diffused via grain boundaries when the grain size becomes larger than the characteristic grain boundary diffusion distance [39,41]. In the B regime, this distance is defined as $L_{gb}^B = \sqrt{\delta D_{gb}} \left(\frac{t}{4D_v}\right)^{1/4}$ [39,41]. Again using data from Refs. [42,43], $L_{gb}^B = 8$ µm after 789 h at 550 °C: $L_{gb}^B > g$, which indicates that diffusion still mostly occurs via grain boundaries at the end of the experiment – this will be reversed at some point if the time exponent of grain growth kinetics is larger than that of L_{gb}^B, 1/4.

4.3 Contributions from grain boundaries and dislocations at 400 °C

The contributions to diffusion are more readily identified in the 400 °C experiment. Indeed, $\sqrt{D_v t}$ is calculated to be 0.05 nm after 48 h at this temperature [42]. It follows that $\sqrt{D_v t} < \delta$, indicating that diffusion is in the C regime (Table 3) and mainly proceeds along grain boundaries and dislocations, with no significant contribution from the bulk. The microstructure in the UFG zone remains approximately constant during the 48 h experiment; based on the relative roles of grain boundaries and dislocations discussed above for the as-deformed material ($t = 0$ in Fig. 16), it is concluded that grain boundary diffusion predominates throughout the experiment. Furthermore, the characteristic grain boundary diffusion distance, $L_{gb}^{C} = \sqrt{D_{gb} t}$, is calculated [43] to be in the range 50–500 nm between 1 and 48 h, while the grain size is around 20 nm: $L_{gb}^{C} > g$, indicating that the contribution from grain boundary diffusion exceeds that from direct bulk diffusion in the overall Cr flux to the surface. The quasi-absence of bulk diffusion is manifested in the flat profiles recorded in the polished specimen, in zones where apparently no short-circuit diffusion was in effect (Fig. 14b and e for example). In contrast, the tub-shaped profiles (Fig. 14c and d for example), which coincide with the depth of UFG material, were caused by short-circuit diffusion in this zone. During this experiment, the alloy formed a Cr_2O_3 scale with a thin NiO layer on the top. It is concluded that the small amount of UFG material at the surface of the polished specimen was effective in promoting the selective oxidation of Cr because oxidation was much slower than it was at 550 °C, and the shallow UFG zone was not consumed by scale growth.

The reason why short-circuit diffusion was in effect in some parts of the specimen and not in others is not evident from the TEM examination: there was no apparent correlation between the shape of the Cr profiles (flat vs tub-shaped) and the local microstructure. More extensive TEM analysis should be carried out where dislocation density and composition profile measurements are systematically associated – although inherent limitations due to the use of thin foils in the TEM will remain.

Another conclusion is made from the profile shapes: lateral diffusion along the metal-oxide interface or via the oxide grain boundaries must have played an important role in selective oxidation. Indeed, the growth of a predominantly Cr_2O_3 scale must be accompanied by Cr loss in the metal, in one form or another. In regions where the composition profiles are flat, the Cr necessary for Cr_2O_3 growth must have come from neighboring zones, via lateral diffusion. In other words, lateral diffusion compensated the diffusivity variations associated with microstructure variations.

Mass balance calculations were done in order to verify whether the composition change in the alloy corresponded to the composition of the oxide scale, along each profile. This is not shown here for the sake of brevity, but we found that the amount of Cr in the oxide and the amount missing in the metal were, in many cases, at variance, confirming that lateral diffusion was significant. In the same way, the fact that the Cr depletion profiles recorded in several locations of the polished specimen after reaction at 550 °C were similar (Fig. 8c) despite large scale thickness variations indicates that lateral diffusion must also have been significant at this temperature.

4.4 Oxidation mechanism

A remarkable aspect of the present experiments is the presence of pores in the polished specimens, within the scale after oxidation at 550 °C (Fig. 6) and at the metal/oxide interface after oxidation at 400 °C (Fig. 12). Such pores have been reported before in the literature, and attributed to the condensation of vacancies produced by the oxidation process (both by the oxidation reaction and via the Kirkendall effect associated with subscale interdiffusion) [45–53]. In contrast, the absence of pores in the ground specimen oxidized at 550 °C illustrates the role of the microstructure in oxidation-induced pore formation. The relatively deep UFG zone in this specimen ensured that a large density of grain boundaries and dislocations was always available near the metal/oxide interface and in the subsurface. The large density of vacancy sinks presumably enhanced the annihilation of oxidation-induced vacancies [54], and avoided their condensation into pores, as proposed in Ref. [51].

Oxidation-induced vacancy generation is thought to play an important role in the formation of two-layer oxide scales observed as a result of non-selective oxidation in a variety of experimental conditions (see [55,56] and refs. therein). In this mechanism, vacancies are generated due to oxidation of the base metal, and oxides of the less-noble element grow in the space made available. Here, the pores observed in the polished specimens were mostly due to the oxidation of the less-noble element, Cr, since the scale was predominantly Cr_2O_3. Interfacial pores below a Cr_2O_3 scale have also been observed previously [57]. In Ref. [57], the authors noted that as oxidation proceeded, Cr oxide, and later Al oxide, grew in the pores. This is consistent with the relative stability of the oxides in the Al-Cr-O-Ni system. In the present case, however, the pores were found to contain Ni oxide (Figs. 6 and 13). This is particularly unexpected in the 400 °C experiment (Fig. 13), where the scale appeared to be compact above the pores. Considering the relative stability of NiO and Cr_2O_3 [58], a compact Cr_2O_3 scale should maintain at the metal surface a p_{O_2} too low for Ni to oxidize. The oxidation of Ni in this context remains unclear at this stage.

5 Conclusions

This work illustrates the role of the microstructure in the beneficial effect of cold work on selective oxidation. The atypical Cr depletion profiles measured here reflect an abrupt change in diffusion properties between the severely deformed subsurface and the bulk, due to increased dislocation and grain boundary densities in the former. Polishing and grinding produce similar defect densities, but the deformation extends much deeper after grinding. The depth of deformed material is found to be critical, as it determines the flux of Cr provided to the surface via fast diffusion before the fast-diffusing material is consumed by oxide growth. As a result, the depth required for surface deformation to be effective increases with the oxidation temperature.

The grain boundary and dislocation densities generated by polishing or grinding are not large enough for the diffusion properties to be uniform within the deformed material either: diffusion fringes from two neighboring defects do not overlap (B regime). It is further concluded that grain boundary diffusion predominates, both compared to dislocation diffusion and to bulk diffusion, in the conditions of interest.

Specifically, the amount of Cr that diffuses to the surface via grain boundaries is larger than that supplied to the surface via the bulk only.

This work highlights the role of dislocation and grain boundary dynamics in oxidation at intermediate temperatures. This aspect is not as relevant at low temperatures, where the microstructure is essentially static in the timescale of laboratory testing, or at high temperatures, where dislocations are annealed out by the time the isotherm stage is reached. In between, however, different kinetic regimes can be in effect, and anticipating the way cold work will affect oxidation requires a detailed knowledge of the microstructure evolution. Together with more complete microstructure data, the present analysis can be used as a preliminary step toward predictive oxidation models.

A major difficulty is that severely deformed microstructures produced by cold-work are not uniform, and do not evolve in a uniform manner during recovery, recrystallization and grain growth (see Figs. 9 and 12 for instance). This may lead to local variations in the oxidation behavior, although the effect is mitigated by lateral diffusion, presumably along the metal-oxide interface or via the oxide grain boundaries. The present results suggest that defect densities and their time evolution should be described as distributions, which would then be used to predict the likelihood of local failure over time. Similarly, the dispersion of grain boundary diffusivities, which is significant even in systems as simple as pure Ni [59], should be factored in. Another aspect which has not been considered in the present paper is the mobility of dislocations and grain boundaries, which plays a role in diffusion [39] and is also subject to dispersion.

Acknowledgements

This work has received funding from the Euratom research and training programme 2014–2018 under Grant Agreement N° 661913 (SOTERIA project). This article reflects only the author's view and the European Commission is not responsible for any use that may be made of the information it contains.

The authors would like to thank S. Bosonnet and K. Ginestar (CEA/DEN/SCCME) for their help setting up the heat treatments, M. Tabarant (CEA/DEN/SEARS) for performing the GDOES analysis, and F. Rouillard (CEA/DEN/SCCME) for stimulating discussions.

Data availability

The raw/processed data required to reproduce these findings cannot be shared at this time due to technical or time limitations.

Appendix

The minimum at. fraction of Cr required for the transition from internal to external Cr_2O_3 formation is given by [34]:

$$N_1 = \left(g^* \frac{\pi}{2\nu} \frac{V_a}{V_{ox}} \frac{N_O^s D_O}{D_{Cr}} \right)^{1/2}, \tag{A1}$$

where g^* is the critical volume fraction of internal oxide at the transition, ν is the number of O atoms per Cr atoms in the oxide ($\nu = 3/2$), V_a and V_{ox} are the alloy and oxide molar volumes (given for one mol of metal, i.e., $V_{ox} = V_{Cr_2O_3}/2$), respectively, D_O and D_{Cr} are the O and Cr diffusion coefficients in the alloy, respectively, and N_O^s is the oxygen at. fraction in the metal at its surface.

In the literature, the calculation is mostly done using $g^* = 0.3$, after the value measured by Rapp in Ag–In alloys at 550 °C [60]. Although volume fractions of internal oxide higher than 0.3 are often found in NiCr alloys, this value will also be used here, by lack of a better estimate. As is customary, it is assumed that the alloy is covered by a NiO scale, and the p_{O_2} at the metal surface is set by the Ni/NiO equilibrium:

$$\mathrm{Ni} + \frac{1}{2}\mathrm{O_2} = \mathrm{NiO}, \tag{A2}$$

$$p_{O_2} = (K_{NiO})^{-2}, \tag{A3}$$

where the activity of Ni in the alloy has been approximated as 1 for simplicity. The equilibrium constant is given by:

$$K_{NiO} = \exp\left(-\frac{\Delta_f G^0_{NiO}}{RT}\right), \tag{A4}$$

where $\Delta_f G^0_{NiO}$ is the standard free energy of formation of NiO. The O content at the metal surface is then obtained from p_{O_2} by Sievert's law:

$$\frac{1}{2}\mathrm{O_2} = \underline{\mathrm{O}}, \tag{A5}$$

$$N_O^s = K_{diss}\left(\frac{p_{O_2}}{p^0}\right)^{1/2}. \tag{A6}$$

with $p^0 = 1$ atm. The dissolution constant is calculated as:

$$K_{diss} = \exp\left(-\frac{\Delta G^0_{diss}}{RT}\right), \tag{A7}$$

where ΔG^0_{diss} is the standard free energy of the dissolution reaction. The temperature dependence of D_O and D_{Cr} is modeled with an Arrhenius law. All parameters used here are given in Table A1.

The minimum at. fraction of Cr required to sustain external Cr_2O_3 growth is given by [35]:

$$N_2 = F\left(\frac{V_a}{V_{ox}}\sqrt{\frac{1}{2}\frac{k_p}{D_{Cr}}}\right) \tag{A8}$$

where again V_{ox} is given for one mol of metal ($V_{ox} = V_{Cr_2O_3}/2$), F is the auxiliary function defined by $F(u) = \sqrt{\pi}u\,(1 - \mathrm{erf}\,u)\exp\left(u^2\right)$ and k_p is the parabolic constant for oxidation, defined with the convention $X^2 = 2k_p t$, with X the oxide thickness. k_p is modeled with an Arrhenius law, with values given in Table A1.

The values obtained for N_1 and N_2 as a function of temperature are plotted in Fig. A1. The graph indicates that using a bulk diffusion coefficient for Cr (and

Table A1: Parameters used in the calculation of the critical Cr content for the transition from internal to external Cr_2O_3 formation, Eq. (A1).

Parameter	Value	Source	Comment
V_a (cm^3/mol)	6.6	[61]	Pure Ni
V_{ox} (cm^3/mol)	14.56	[61]	$\frac{1}{2}Cr_2O_3$
$\Delta_f G^0_{NiO}$ (J/mol)	$-234345 + 84.3 \cdot T$	[58]	
ΔG^0_{diss} (J/mol)	$-182000 + 107.6 \cdot T$	[62]	O in pure Ni
D_O (cm^2/s)	$0.049 \exp\left(-\frac{164000}{RT}\right)$	[62]	O in pure Ni
D_{Cr} (cm^2/s)	$0.74 \exp\left(-\frac{279000}{RT}\right)$	[42]	Cr in Ni–20Cr
k_p (cm^2/s)	$5 \times 10^{-6} \exp\left(-\frac{165000}{RT}\right)$	Own assessment based on Cr_2O_3 thicknesses in Refs. [63,64] and present work	

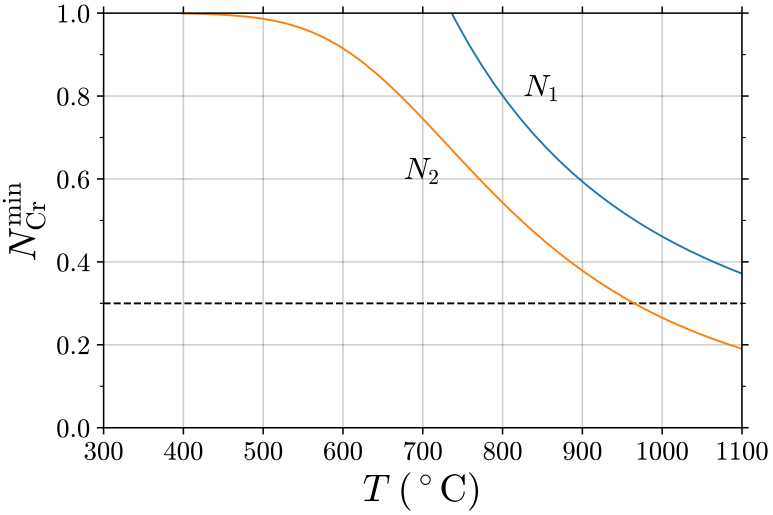

Figure A1: Minimum Cr atom fraction required for the transition from internal to external Cr_2O_3 formation (N_1) and for maintained external Cr_2O_3 growth (N_2). See details in text.

with a number of simplifying assumptions), both values are much higher than the Cr concentration in a Ni–30Cr alloy at the temperatures of interest (300–600 °C). A Ni–30Cr alloy would therefore be expected to undergo non-selective oxidation. (Specifically, a Ni–30Cr alloy would be expected to form internal Cr_2O_3 and external NiO; why internal Cr_2O_3 was not observed here in the polished specimens is not clear at this stage.)

References

[1] K. Lu, J. Lu, Surface nanocrystallization (SNC) of metallic materials-presentation of the concept behind a new approach, J. Mater. Sci. Technol. 15 (1999) 193–197.
[2] T. Wang, J. Yu, B. Dong, Surface nanocrystallization induced by shot peening and its effect on corrosion resistance of 1Cr18Ni9Ti stainless steel, Surf. Coat.

Technol. 200 (2006) 4777–4781.
[3] S. Wang, Y. Hu, K. Fang, W. Zhang, X. Wang, Effect of surface machining on the corrosion behaviour of 316 austenitic stainless steel in simulated PWR water, Corros. Sci. 126 (2017) 104–120.
[4] F.J. Humphreys, M. Hatherly, Recrystallization and Related Annealing Phenomena, Second Edition, Elsevier, Oxford, 2004.
[5] C.S. Giggins, F.S. Pettit, Effect of alloy grain-size and surface deformation on selective oxidation of chromium in Ni-Cr alloys at temperatures of 900 degrees and 1100 degrees C, Trans. Metall. Soc. Aime. 245 (1969) 2509–2514.
[6] T. Ericsson, A study of the Cr-depleted surface layers formed on four Cr-Ni steels during oxidation in steam at 600 °C and 800 °C, Oxid. Met. 2 (1970) 16.
[7] S. Leistikow, I. Wolf, H.J. Grabke, Effects of cold work on the oxidation behavior and carburization resistance of alloy 800, Mater. Corros. 38 (1987) 556–562.
[8] C. Ostwald, H.J. Grabke, Initial oxidation and chromium diffusion. I. Effects of surface working on 9–20% Cr steels, Corros. Sci. 46 (2004) 1113–1127.
[9] R. Naraparaju, H.-J. Christ, F.U. Renner, A. Kostka, Effect of Shot-peening on the Oxidation Behaviour of Boiler Steels, Oxid. Met. 76 (2011) 233.
[10] J. Yuan, X. Wu, W. Wang, S. Zhu, F. Wang, The Effect of Surface Finish on the Scaling Behavior of Stainless Steel in Steam and Supercritical Water, Oxid. Met. 79 (2013) 541–551.
[11] M.R. Ardigo-Besnard, I. Popa, O. Heintz, R. Chassagnon, M. Vilasi, F. Herbst, P. Girardon, S. Chevalier, Effect of surface finishing on the oxidation behaviour of a ferritic stainless steel, Appl. Surf. Sci. 412 (2017) 196–206.
[12] V. Parry, A. Col, C. Pascal, Beneficial effect of cold-working on high temperature oxidation resistance of austenitic stainless steel, Corros. Sci. (2019) 108149.
[13] J.C. Langevoort, T. Fransen, P.J. Geilings, On the influence of cold work on the oxidation behavior of some austenitic stainless steels: High temperature oxidation, Oxid. Met. 21 (1984) 271–284.
[14] G.J. Yurek, D. Eisen, A. Garratt-Reed, Oxidation behavior of a fine-grained rapidly solidified 18–8 stainless steel, Metall. Trans. A. 13 (1982) 473–485.
[15] R.A. Holm, H.E. Evans, The resistance of 20Cr/25Ni steels to carbon deposition. 3. Cold work and selective preoxidation, Mater. Corros. 38 (1987) 219–224.
[16] X. Peng, J. Yan, Y. Zhou, F. Wang, Effect of grain refinement on the resistance of 304 stainless steel to breakaway oxidation in wet air, Acta Mater. 53 (2005) 5079–5088.
[17] J.-H. Kim, D.-I. Kim, S. Suwas, E. Fleury, K.-W. Yi, Grain-Size Effects on the High-Temperature Oxidation of Modified 304 Austenitic Stainless Steel, Oxid. Met. 79 (2013) 239–247.
[18] D. Caplan, Effect of cold work on the oxidation of FeCr alloys in water vapour at 600 °C, Corros. Sci. 6 (1966) 509–515.
[19] M. Payet, L. Marchetti, M. Tabarant, J.-P. Chevalier, Corrosion mechanism of a Ni-based alloy in supercritical water: Impact of surface plastic deformation, Corros. Sci. 100 (2015) 47–56.
[20] M. Payet, L. Marchetti, M. Tabarant, F. Jomard, J.-P. Chevalier, Corrosion mechanisms of 316L stainless steel in supercritical water: The significant effect of work hardening induced by surface finishes, Corros. Sci. 157 (2019) 157–166.
[21] I.G. Wright, R.B. Dooley, A review of the oxidation behaviour of structural alloys in steam, Int. Mater. Rev. 55 (2010) 129–167.

[22] V. Trindade, H.-J. Christ, U. Krupp, Grain-Size Effects on the High-Temperature Oxidation Behaviour of Chromium Steels, Oxid. Met. 73 (2010) 551–563.
[23] R.P. Oleksak, G.R. Holcomb, C.S. Carney, L. Teeter, Ö.N. Doğan, Effect of Surface Finish on High-Temperature Oxidation of Steels in CO_2, Supercritical CO_2, and Air, Oxid. Met. 92 (2019) 525–540.
[24] S. Cissé, L. Laffont, B. Tanguy, M.-C. Lafont, E. Andrieu, Effect of surface preparation on the corrosion of austenitic stainless steel 304L in high temperature steam and simulated PWR primary water, Corros. Sci. 56 (2012) 209–216.
[25] F. Carrette, Relâchement des produits de corrosion des tubes en alliage 690 de générateur de vapeur du circuit primaire des réacteurs à eau pressurisée, PhD thesis, Toulouse, INPT, 2002. http://www.theses.fr/2002INPT014G (accessed November 30, 2019).
[26] D. Morton, N. Lewis, M. Hanson, S. Rice, P. Sanders, Nickel Alloy Primary Water Bulk Surface and SCC Corrosion Film Analytical Characterization and SCC Mechanistic Implications. United States: N. p., 2007. https://doi.org/10.2172/903204 (accessed March 1st, 2020).
[27] Z. Zhang, J. Wang, E.-H. Han, W. Ke, Analysis of Surface Oxide Films Formed in Hydrogenated Primary Water on Alloy 690TT Samples With Different Surface States, J. Mater. Sci. Technol. 30 (2014) 1181–1192.
[28] H. Ming, Z. Zhang, J. Wang, R. Zhu, J. Ding, J. Wang, E.-H. Han, W. Ke, Effect of surface state on the oxidation behavior of welded 308L in simulated nominal primary water of PWR, Appl. Surf. Sci. 337 (2015) 81–89.
[29] S.E. Ziemniak, M. Hanson, P.C. Sander, Electropolishing effects on corrosion behavior of 304 stainless steel in high temperature, hydrogenated water, Corros. Sci. 50 (2008) 2465–2477.
[30] K.B. Fisher, B.D. Miller, E.C. Johns, E.A. Marquis, The role of surface deformation in the oxidation response of type 304 SS in high temperature deaerated water, Corros. Sci. 141 (2018) 88–96.
[31] S. Lozano-Perez, D.W. Saxey, T. Yamada, T. Terachi, Atom-probe tomography characterization of the oxidation of stainless steel, Scr. Mater. 62 (2010) 855–858.
[32] S. Lozano-Perez, K. Kruska, I. Iyengar, T. Terachi, T. Yamada, The role of cold work and applied stress on surface oxidation of 304 stainless steel, Corros. Sci. 56 (2012) 78–85.
[33] T. Moss, G. Cao, G.S. Was, Oxidation of Alloy 600 and Alloy 690: Experimentally Accelerated Study in Hydrogenated Supercritical Water, Metall. Mater. Trans. A. 48 (2017) 1596–1612.
[34] C. Wagner, Reaktionstypen bei der Oxydation von Legierungen, Z. Elektrochem. 63 (1959) 772–790.
[35] C. Wagner, Theoretical analysis of the diffusion processes determining the oxidation rate of alloys, J. Electrochem. Soc. 99 (1952) 369–380.
[36] J. Philibert, Atom movements - Diffusion and mass transport in solids, Les Editions de Physique, Les Ulis, 1991.
[37] J.-O. Andersson, T. Helander, L. Höglund, P. Shi, B. Sundman, Thermo-Calc & DICTRA, computational tools for materials science, Calphad. 26 (2002) 273–312.
[38] L.G. Harrison, Influence of dislocations on diffusion kinetics in solids with particular reference to the alkali halides, Trans. Faraday Soc. 57 (1961) 1191–1199.
[39] I. Kaur, Y. Mishin, W. Gust, Fundamentals of Grain and Interphase Boundary Diffusion, 3rd ed., Wiley, 1995.

[40] H. Mehrer, Diffusion in Solids, Springer Berlin Heidelberg, Berlin, Heidelberg, 2007.
[41] Y. Mishin, C. Herzig, Diffusion in fine-grained materials: Theoretical aspects and experimental possibilities, Nanostructured Mater. 6 (1995) 859–862.
[42] T. Gheno, F. Jomard, C. Desgranges, L. Martinelli, Tracer diffusion of Cr in Ni and Ni-22Cr studied by SIMS, Materialia. 3 (2018) 145–152.
[43] J. Čermák, Grain boundary self-diffusion of 51Cr and 59Fe in austenitic Ni-Fe-Cr alloys, Mater. Sci. Eng. A. 148 (1991) 279–287.
[44] G. Stechauner, E. Kozeschnik, Assessment of substitutional self-diffusion along short-circuit paths in Al, Fe and Ni, Calphad. 47 (2014) 92–99.
[45] M.G.C. Cox, B. McEnaney, V.D. Scott, Vacancy condensation and void formation in duplex oxide scales on alloys, Philos. Mag. 28 (1973) 309–319.
[46] R.E. Smallman, P.S. Dobson, The behaviour of metal lattice vacancies during oxidation, in: Surface and Defect Properties of Solids, Volume 4, J. M. Thomas and M. W. Roberts, eds, 1975, pp. 103–125.
[47] G.B. Gibbs, R. Hales, Influence of metal lattice vacancies on oxidation of high-temperature materials, Corros. Sci. 17 (1977) 487–507.
[48] F. Gesmundo, P.Y. Hou, Analysis of Pore Formation at Oxide–Alloy Interfaces—II: Theoretical Treatment of Vacancy Condensation for Immobile Interfaces, Oxid. Met. 59 (2003) 63–81.
[49] V. Maurice, G. Despert, S. Zanna, M.-P. Bacos, P. Marcus, Self-assembling of atomic vacancies at an oxide/intermetallic alloy interface, Nat. Mater. 3 (2004) 687–691.
[50] S. Perusin, B. Viguier, D. Monceau, L. Ressier, E. Andrieu, Injection of vacancies at metal grain boundaries during the oxidation of nickel, Acta Mater. 52 (2004) 5375–5380.
[51] C. Desgranges, F. Lequien, E. Aublant, M. Nastar, D. Monceau, Depletion and Voids Formation in the Substrate During High Temperature Oxidation of Ni–Cr Alloys, Oxid. Met. 79 (2013) 93–105.
[52] C.-M. Wang, A. Genc, H. Cheng, L. Pullan, D.R. Baer, S.M. Bruemmer, In-Situ TEM visualization of vacancy injection and chemical partition during oxidation of Ni-Cr nanoparticles, Sci. Rep. 4 (2014).
[53] R.P. Oleksak, M. Kapoor, D.E. Perea, G.R. Holcomb, Ö.N. Doğan, The role of metal vacancies during high-temperature oxidation of alloys, Npj Mater. Degrad. 2 (2018) 25.
[54] B. Pieraggi, R.A. Rapp, Stress generation and vacancy annihilation during scale growth limited by cation vacancy diffusion, Acta Metall. 36 (1988) 1281–1289.
[55] L. Martinelli, F. Balbaud-Célérier, A. Terlain, S. Bosonnet, G. Picard, G. Santarini, Oxidation mechanism of an Fe–9Cr–1Mo steel by liquid Pb–Bi eutectic alloy at 470°C (Part II), Corros. Sci. 50 (2008) 2537–2548.
[56] F. Rouillard, G. Moine, L. Martinelli, J.C. Ruiz, Corrosion of 9Cr Steel in CO_2 at Intermediate Temperature I: Mechanism of Void-Induced Duplex Oxide Formation, Oxid. Met. 77 (2012) 27–55.
[57] R.P. Oleksak, C.S. Carney, G.R. Holcomb, Ö.N. Doğan, Structural Evolution of a Ni Alloy Surface During High-Temperature Oxidation, Oxid. Met. 90 (2018) 27–42.
[58] D.J. Young, High temperature oxidation and corrosion of metals, Elsevier, Amsterdam, 2008.

[59] T. Gheno, F. Jomard, C. Desgranges, L. Martinelli, Grain boundary diffusion of chromium in polycrystalline nickel studied by SIMS, Materialia. 6 (2019) 100283.
[60] R.A. Rapp, The transition from internal to external oxidation and the formation of interruption bands in silver-indium alloys, Acta Metall. 9 (1961) 730–741.
[61] Physical Constants of Inorganic Compounds, in: CRC Handb. Chem. Phys., 91st ed., CRC Press/Taylor and Francis, Boca Raton, USA, 2011.
[62] J.W. Park, C.J. Altstetter, The diffusion and solubility of oxygen in solid nickel, Metall. Trans. -Phys. Metall. Mater. Sci. 18 (1987) 43–50.
[63] T. Gheno, Oxidation and carburisation of model chromia-forming alloys in carbon dioxide, Phd thesis, UNSW (Sydney, Australia)/INPT (Toulouse, France), 2012. http://ethesis.inp-toulouse.fr/archive/00001990/ (accessed March 1st, 2020).
[64] E. Schmucker, C. Petitjean, L. Martinelli, P.-J. Panteix, S. Ben Lagha, M. Vilasi, Oxidation of Ni-Cr alloy at intermediate oxygen pressures. I. Diffusion mechanisms through the oxide layer, Corros. Sci. 111 (2016) 474–485.